

Article

Wildfire Pyroconvection and CAPE: Buoyancy's Drying and Atmospheric Intensification—Fort McMurray

Atoossa Bakhshaii ^{1,*}, Edward A. Johnson ¹ and Kiana Nayebi ²

¹ Department of Biological Sciences, University of Calgary, Calgary, AB T2N 1N4, Canada; Johnsone@ucalgary.ca

² Department of Natural Sciences, University of Calgary, Calgary, AB T2N 1N4, Canada; kiana.Nayebi@gmail.com

* Correspondence: atoossa.bakhshaii@ucalgary.ca

Received: 27 May 2020; Accepted: 15 July 2020; Published: 18 July 2020



Abstract: The accurate prediction of wildfire behavior and spread is possible only when fire and atmosphere simulations are coupled. In this work, we present a mechanism that causes a small fire to intensify by altering the atmosphere. These alterations are caused by fire-related fluxes at the surface. The fire plume and fluxes increase the convective available potential energy (CAPE) and the chance of the development of a strong pyroconvection system. To study this possible mechanism, we used WRF-Fire to capture fire line propagation as the result of interactions between heat and moisture fluxes, pressure perturbations, wind shear development and dry air downdraft. The wind patterns and dynamics of the pyroconvection system are simulated for the Horse River wildfire at Fort McMurray, Canada. The results revealed that the updraft speed reached up to 12 m/s. The entrainment mixed the mid and upper-level dry air and lowered the atmospheric moisture. The mid-level and upper-level dew point temperature changed by 5–10 °C in a short period of time. The buoyant air strengthened the ascent as soon as the nocturnal inversion was eliminated by daytime heating. The 887 J/kg total increase of CAPE in less than 5 h and the high bulk Richardson number (BRN) of 93 were indicators of the growing pyro-cumulus cell. The presented simulation has not improved the original model or supported leading-edge numerical weather prediction (NWP) achievements, except for adapting WRF-Fire for Canadian biomass fuel. However, we were able to present a great deal of improvements in wildfire nowcasting and short-term forecasting to save lives and costs associated with wildfires. The simulation is sufficiently fast and efficient to be considered for a real-time operational model. While the project was designed and succeeded as an NWP application, we are still searching for a solution for the intractable problems associated with political borders and the current liable authorities for the further development of a new generation of national atmosphere–wildfire forecasting systems.

Keywords: wildfire; pyroconvection; weather; Skew-T

1. Introduction

Climate and weather impact the frequency and behavior of wildfires [1,2]. Wildfires also provide substantial short and long-term feedbacks to the atmosphere and land-surface [3]. The burning of biomass increases the output of emission products, heat and water vapor fluxes into the atmosphere; the short-term impact on the atmosphere is an immediate small-scale fire caused by local heat and moisture fluxes such as fire winds and pyro-cumulus clouds. Long-term atmospheric cooling can be caused by indirect and direct atmospheric aerosol radiative scattering or warming caused by released greenhouse gases such as carbon monoxide, methane and nitrous oxide [4–7]. Every year, global fires directly emit 200–300 Gkg(= 10^{15} g) of carbon into the atmosphere [7]. Emissions from Canadian

boreal biomass burning have regularly been observed in the upper troposphere and even in the lower stratosphere over Europe and the USA [8]. Our capacity to understand and manage wildfires will remain imperfect as long as our knowledge is confined by our limited observation and restricted understanding of wildfire mechanisms. One of the areas that requires investigation is the transition of a wildfire to a large fire with a high intensity, spread and burned area. The current study offers a numerical simulation case-study and discussion of the dynamics and physics of the transition of wildfire to pyroconvection. The research also suggests that a coupled atmosphere–fire prediction system could provide additional guidance for decision-makers.

Certain atmospheric conditions can result in excessive fuel drying and extreme pyroconvection activities [9]. Moisture in the mid-atmosphere tends to be resilient to rapid changes in the absence of dry/moist large-scale advection [10,11], while wildfire can change the atmosphere moisture content rapidly [12]. A lack of wildfire–atmosphere heat and moisture interaction can throw off any non-coupled weather or wildfire forecasts.

The wildfires associated with pyroconvection behavior cannot be predicted by a simple two-dimensional physical or semi-physical spread model. Although the simplified fire spread models are a useful measure of fire front spread on the ground in the absence of the forceful and rapid changes in the wind and moisture of the atmosphere boundary layer, they cannot foresee the time and location of occurrence of pyroconvection and extreme forces.

Primary knowledge [13] of mesoscale convection systems (MCSs) suggests three requirements for the development of deep convections: (1) instability, (2) an abundance of boundary layer moisture and (3) a lifting mechanism (trigger) to produce vertical motion, allowing a parcel to attain free convection. The requirements are fundamental to the development of all MCSs (or pyroconvection mesoscale convection systems, PMCSs) from short-lived single cells to destructive supercells. What separates the environments of varying storm types from each other is the vertical wind shear within the pre-storm environment. Buoyancy primarily determines the updraft strength, and wind shear determines the storm evolution [13]. Wildfire surface heating can act as a trigger, allowing free convection and adding moisture (via fuel combustion) to the air in a short period of time, which will increase buoyancy. Wildfires can modify the pre-existing environment toward a favorable deep convection condition by warming and moistening the lowest level of the stratosphere.

The pyroconvection grows with very strong winds which change directions and drive with lateral vorticity and vertical wind shear. Badlan et al. [14] performed an idealized numerical simulation to study the role of deep flaming in pyroconvection by using WRF-Fire version 3.9. They repeated the simulation with variations of fire intensities, spatial extensions and horizontal resolutions and three different atmospheric profiles to explore the dynamics of pyroconvection. These simplified simulations gave an informative insight into the dynamics of pyroconvection without considering the moisture fluxes. Lareau and Clements [12] showed the atmospheric vertical thermodynamics and dynamics profile, and the daily variation had a significant impact on the onset and development of pyroconvection, as the wildfire moisture and heat fluxes from below were shown to be able to expedite the process. They established direct observations using a scanning Doppler light detection and ranging (LiDAR) and mobile radiosonde system during two large wildfires in northern California. The results suggested that the plume condensation level was substantially higher than the ambient lifting condensation level (LCL), which implies that the lifting air in the fire plume reflects the actual properties of the lower plume. The plume must be cooled largely near its base due to entrainment as it decays towards adiabatic ascent higher up the convective condensation level (CCL).

To examine the transition process of a wildfire to a pyroconvection, we chose to study the early stages of the Horse River wildfire which eventually burned an area of 589,522 hectares. The emissions from the Horse River fire had a pronounced impact on the measured annual concentrations and health monitoring sites (NH_3 was up to 14 times higher than non-fire impacted periods for some pollutants) [6].

We are interested in the first days of the event because that is when the fire made the first transition to pyroconvection. We simulated the fire in hindcast mode using the numerical weather and fire prediction model. The choice of model depends on the questions at hand and the availability of the model and resources. After some investigations, we used WRF-Fire [15].

The objective of this paper is to investigate the transition of a wildfire to a large wildfire and the initiation of pyroconvection. We also investigate the practicality of predicting a large fire. We study the transition mechanism by using WRF 3.9.1. We present a Horse River wildfire (Fort McMurray, Alberta Canada) hindcast simulation, as well as our results, with a focus on atmosphere profiles and storm onset. The current research is not an observational or numerical advancement to wildfire models; it is rather an application and a study on the practicality and efficacy of wildfire forecasts. Lastly, we discuss the existing challenges to a fully functional operational coupled atmospheric–wildfire forecast system.

2. Horse River Wildfire 2016

The 2015–16 El Niño (NOAA El Niño Advisories) caused a warmer winter over Canada, at almost 5 °C warmer than the climatological average across all provinces. The 2016 spring remained warmer and drier than the normal climate in western Canada and the Prairies, while an inflow of cold Arctic air brought colder than normal temperatures over eastern and northeastern Canada. The average precipitation for the period 1981–2010 for Fort McMurray in July was 80.7 mm and the maximum temperature was 24 °C. Fort McMurray international airport weather station recorded winter temperatures which were about 4 °C warmer than normal in 2015–2016, while precipitation was around half that of the normal records. This led to an extremely dry biomass condition combined with gusty winds at the beginning of May, creating critical conditions for wildfire with extreme fire danger indices in the area on May 1, 2016. The subject area is located in the northeast of Alberta, south-west of Fort McMurray. The city is in the middle of the Athabasca oil sands, surrounded by boreal forest of white spruce, jack pine, trembling aspen and peatlands. The overall topography of the area is relatively flat, while the four rivers that pass through the city of Fort McMurray create slopes with riparian vegetation of white spruce and balsam fir.

A severe wildfire in May 2016 led to the largest evacuation in the history of Canada and caused widespread damage. There were five active fires between April 29 and May 1, 2016 in the area. Four of them were within close distances from the populated area of the city of Fort McMurray; those fires (MMD001-004) were suppressed and controlled by Alberta Fire crews less than a day after their ignitions. The Horse River fire (identified by MWF009-16) started in the south of the city and swept through the city in less than 72 h. It destroyed over 2400 homes and buildings. It continued to spread across Alberta and into Saskatchewan. The Horse River fire started on May 1, 2016, and a mandatory evacuation was issued on May 3. The fire spread reached 30 to 40 m per minute and created fire-driven weather patterns and winds at its peak. The satellite image from the second day of the fire displayed the pyro-cumulus clouds. The burned area stretched west and east towards the Saskatchewan border, covering 589,552 hectares. The wildfire was declared to be under control on 4 July 2016 after burning for 65 days. During the fire, the lack of knowledge regarding the wind direction (due to the coarse observation and weather forecast biases) made it difficult to predict the fire behavior. The forecast uncertainty was large, which was partially due to fire wind modification and associated heat fluxes. The scientific questions regarding the fire are the following: What was the main trigger that unleashed the Horse River fire (MWF009-16)? What was the main difference between the Horse River fire and the other four fires in the area that had been suppressed? and could we have predicted the Horse River wildfire in a timely manner? To answer these questions, we examine the weather and fire as one system.

3. Methods

The WRF model is an upgrade of the fifth-generation NCAR/Penn State Mesoscale Model (MM5), and the fire module runs in large eddy simulation (LES) mode [16,17]. While WRF-Fire has been launched as a research and operational model in the USA and other countries [15], we could not make use of it in Canada. The problem is that the current Canadian biomass fuel classification is not compatible with the original WRF-Fire biomass classes. With some modifications and assumptions, we adjusted the Canadian digital biomass fuel classification map to be compatible with WRF-Fire and its fire module. Appendix A describes the technical modification of WRF-Fire for the Canadian digital biomass fuel map. The Horse River wildfire was simulated using a two-way interaction of the fire and the atmosphere. The case study was also fast and efficient computationally for real-time operational forecasts. Next, we briefly explain the case study area, data, the Canadian digital fuel map and finally the result and discussion of the case study. The Supplementary Materials provide the technical modifications of WRF-Fire for the Canadian digital biomass fuel map and the case study domains in detail.

3.1. Data

Initial and boundary conditions are required to start any environmental simulation. For the weather prediction/hindcast in a limited area, we used GFS (Global Forecast System by the National Centers for Environmental Prediction (NCEP)) analysis, which is publicly available. The resolution of GFS is very coarse for the fire spread algorithm in WRF-Fire, where the fire module requires a horizontal sub-grid resolution of 35 m² or lower. To achieve such a fine resolution, we used the two-way nested simulation (multiple domains at different grid resolutions run simultaneously and communicate with each other). The coarser domain provided the initial and boundary conditions for the inside smaller domain (nest). The model ran multiple domains at multiple nested levels (telescoping) to produce very fine boundary conditions for the interior domain—i.e., a 200 m² grid space resolution—where the fire ignited. We considered five two-way nested domains with 27,000, 9000, 3000, 1000 and 200 m² grid space resolutions. To remain confined within the assumption that has been made by the fire-spread model [18], we defined the sub-grid resolution scale with a ratio of 0.1 of the inner WRF's domain resolution (sub-grid resolution of 20 m² from 200 m² resolution of the inner WRF domain). Figure 1 shows the five WRF domains at the most inner domain. The inner domain presents the area in which the wildfire spread model interacts with the other weather domains.

In addition to weather data, the fire module requires fuel data and very fine resolution topography compatible with a sub-grid resolution. We added the digital elevation map from the Atlas of Canada (<https://www.nrcan.gc.ca/home>) with a horizontal resolution of 20 m². Natural Resources of Canada provided us the available digital fuel map for Canada with a resolution of 250 m². The Canadian digital fuel map has a slightly different classification for the variety of vegetation compared to the US digital map [19] which had been originally adopted in WRF-Fire (SFIRE). We modified the WRF-Fire “firenamelist” for the Canadian fuel classification (see the Supplementary Materials).

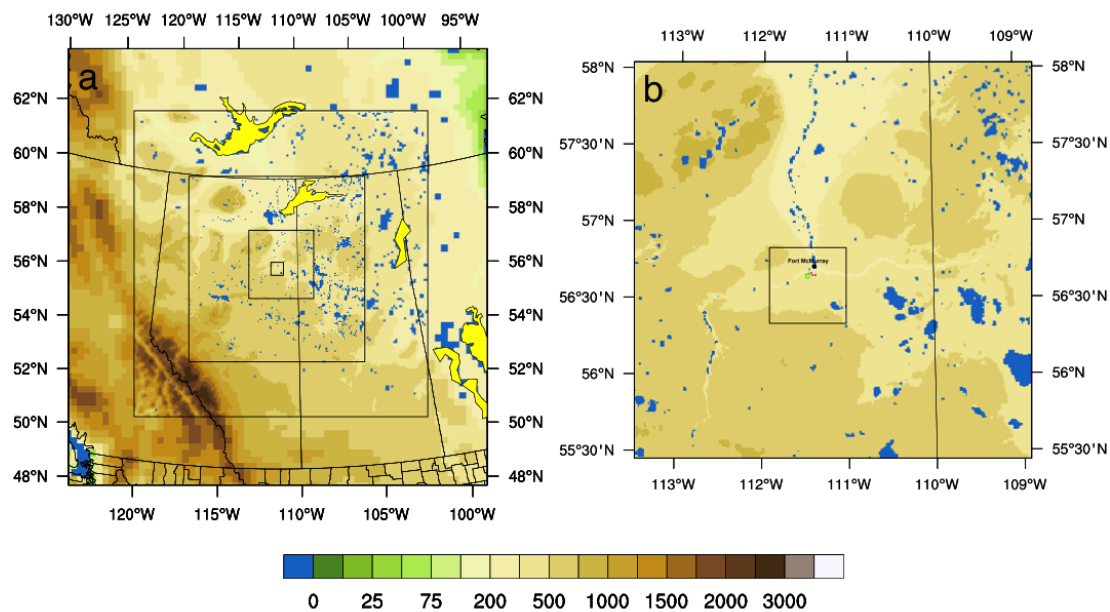


Figure 1. (a) The left figure shows five WRF domains and (b) the right figure shows two inner domains. The inner domain also presents the fire domain. The background color represents the elevation map, lakes are represented in solid yellow and the blue color shows the surface waters including rivers.

3.2. Observation

We used fire hotspots from FIRM (Fire Information for Resource Management System, <https://earthdata.nasa.gov/firms>) for ignitions, using MODIS (Moderate Resolution Imaging Spectroradiometer) Collection 6 NRT (near real-time, less than 3 h from the acquisition time) and VIIRS (Visible Infrared Imaging Radiometer Suite) hotspot data. The thermal anomalies/active fires represent any place within a 1 km pixel that is flagged by the MODIS Fire and Thermal Anomalies algorithm [20] as containing one or more fires within the pixel. This is the most basic fire product, in which active fires and other thermal anomalies, such as volcanoes, are identified as early as 3 h after acquisitions. The VIIRS Active Fire detection product is based on the instrument's 375 m nominal resolution data. MODIS and VIIRS are multi-disciplinary sensors on-board NOAA and NASA Satellites (Terra, Aqua, Suomi-NPP). The earliest NRT (Figures 2 and 3) hotspots in the Fort McMurray wildfire were detected by the Terra satellite with the MODIS instrument at 3:51 and 5:29 UTC (MDT+7) on May 2, 2016. The data from the Terra satellite on May 2 were not from the first pass, but they were from the first NRT remote observation. All captured data cannot be processed immediately. The processing requires spacecraft housekeeping data and predicted ephemeris. The VIIRS instrument aboard the joint NASA/NOAA Suomi National Polar-Orbiting Partnership (Suomi-NPP) satellite passed after MODIS. Hotspot locations were obtained from multiple sources including MODIS, VIIRS and AVHRR (Advanced Very-High-Resolution Radiometer) sensors. The strength of these satellite systems lies in their time-series of daily multi-spectral observations, which are used to characterize and monitor the land surface from regional to global scales. Near real-time (NRT) fire products are generated within approximately 3 h of satellite observations to meet the needs of the applicable community. There are five AVHRR satellites providing hotspots via NOAA's Fire Identification, Mapping and Monitoring Algorithm (FIMMA) which are publicly available 3–6 h after acquisitions. We considered FIRM to represent the earliest detections to examine the potential of real-time forecasting as well.

Although each spot represents almost a 1 km gridded pixel, this does not mean that the fire covered the entire grid-cell. We consider a 25 m radius from the center of the hotspot for each ignition. We also used burned area images for 24 h fire perimeter evaluation. When vegetation burns, the burned area or fire-affected areas become characterized by deposits of charcoal and ash; fire removes vegetation or alters the vegetation structure. If soil is exposed after a fire, the brightness

in Band 1 will slightly increase, but that may be offset by the presence of black carbon residue. MODIS (Terra) Land Surface Reflection (Bands 7, 2, 1 and Band 1-2-1) products are provided by NASA WORLDVIEW (<https://worldview.earthdata.nasa.gov>). We used the MODIS Land Surface Reflectance products available from both the Terra (MOD09) and Aqua (MYD09) satellites. The sensor resolution was up to 250 m (the imagery resolution is 250 m) and the temporal resolution was daily. As burned area products do not have a fine temporal resolution (daily images), it was not possible to evaluate the hourly location of the fire perimeter via satellite products. There was also no access to the actual fire perimeter from in situ observations (a very common observational problem). Therefore, the observations would only be sufficient for overall (daily) verification.

The only weather station close to the area of study located at Fort McMurray airport (YMM). Unfortunately, the station is far from the location of the fire, and the event date has many missing records in time. The recently released report (WMF009-2016, completed April 2017) demonstrates that the fire was reported at 16:02 on May 1. The WRF ignition algorithm uses the hotspots (the only available data at the time of simulation and the earliest available data with the current arrangement) found 5 h after the ground-based detection. This case is a prime example of the importance of collaboration in the multi-levels of provincial, national and international authorities. The M009-16 report also demonstrated that the fire was a crown fire with a speed of 10 m/min at the time. The real ignition time was not discussed in the report. However, we suspect that the ignition did not start long before detection, namely 1–2 h earlier. The daily burned area map provided by the report shows that the fire start location progressed toward the west on May 1 and then turned toward the east later on May 2. The daily changes in the burned area were driven by the wind direction changes.

4. Results

The Fort McMurray event was the costliest natural disaster in Canada and a fitting case to investigate the viability and serviceability of using a simulation to save lives and costs associated with a wildfire. However, this was also a difficult case to study due to the limited data, which is a common issue in extreme events. During this study, the only available data included the satellite images, hotspots and total daily burned area images. The WRF-Fire simulation was set up for five domains (Figure 1) for a period (lead time) of 24 h. The 24 h hindcast simulation took 6 h to complete using 144 computational processing units (CPUs). The reasonably fast performance shows the functionality of the model for real-time forecasts. The simulation started a few hours before the fire, early on May 3. The final stage of simulation at the time of pyroconvection onset is presented here. Figure 2 is an illustration of hotspots, reported fires and vertical profile locations. The vertical profile location is in the vicinity of the fire front on May 3. The model wind speed output is illustrated in Figure 3. Wind speed increased in the burned area and reached its maximum where the heat flux was at maximum, as illustrated in Figure 3b. The convergence and divergence became visible and more pronounced in the finer-resolution inner domains. Figure 3a demonstrates the 1 km resolution wind at 10 m above-ground at 00 UTC on May 3, 2016. Figure 3b simultaneously shows the 200 m resolution wind speed and direction. The comparison of the two images shows that the wind speed at the burned area was up to 3 times faster than the surrounding environmental wind speed.



Figure 2. Location of hotspots and acquisition times of the reported fire. The question mark is the start point of the burned area at the time of reporting by the MWF009. The white arrow is the location of the model atmosphere profiles. Credit: Google Earth.

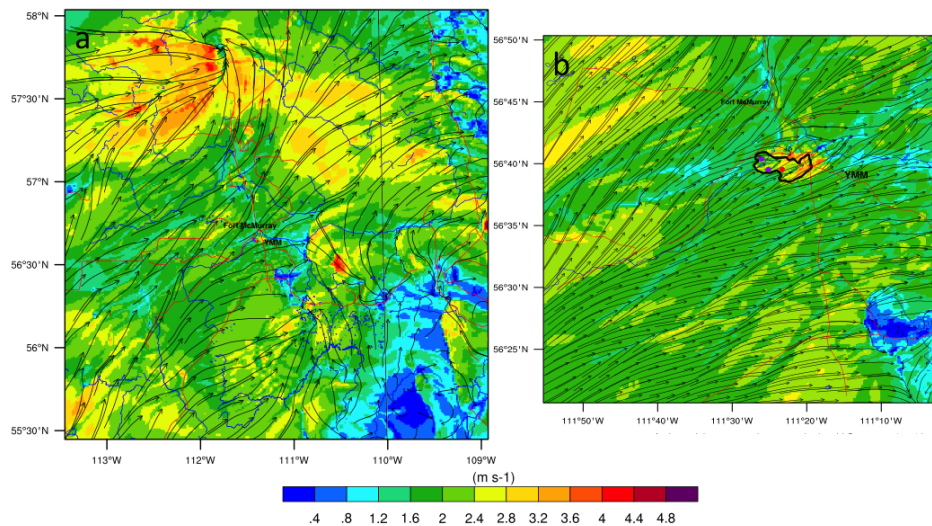


Figure 3. Wind speed and direction at 10 m above the ground from WRF outputs at 00 UTC on May 3, 2016. (a) The left image is 1 km resolution outputs and (b) uses a 200 m grid space resolution. The three purple (earlier) and red (later) dots are ignitions from hotspots within the model. The model burned area at 00 UTC on May 3, 2016 is presented by the thick black line.

Figure 4 is a 3D illustration of the vertical wind speed (updraft). The north–south view of Fort McMurray city demonstrates many up and down draft cells in the burned area. The strongest updraft is presented in red, and downdrafts are in the blue spectrum. The vertical velocities between -1 to 1 m/s were eliminated by the reduction of color transparency in this figure, allowing a better presentation of severe pyroconvection updrafts. Rising air occurs in the region of maximum vorticity, and sinking air is associated with negative vorticities. The next figures shows variational views at the location of the strongest model output for updraft.

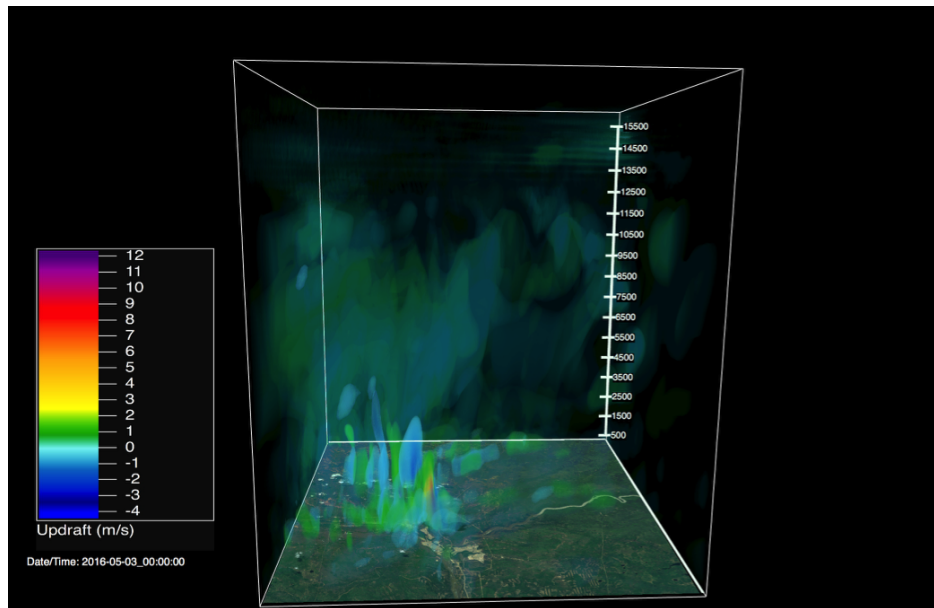


Figure 4. Updrafts and downdrafts at 00 UTC on May 3, 2016. The box is 55 km on each side and is 16 km tall. The blue colors are downdrafts and bright colors are updrafts. The box represents the fire domain and the finest resolution of the model at 200 m. The wind speed color transparency is weighted to present a more transparent area for speeds between -1 to 1 m/s. Image produced by VAPOR (www.vapor.ucar.edu).

Figure 5 is a thermo-diagram (Skew-T diagram) of model outputs at the location of 56.69° N and 111.39° W (a few kilometers to the north of the burned area). The thermo-diagram shows a well-established environmental convective available potential energy (CAPE) by 00 UTC on May 3. Figure 6 shows two thermo-diagrams at the same location but at a different time to show the atmosphere profile changes due to daily warming and synoptic forces. The simulation demonstrated a rapid change in environmental CAPE starting at 18 UTC on May 2. The CAPE reached 887 J/kg in less than 5 h (Figures 5 and 6b). The unstable atmosphere was caused by the diurnal heating and moistening of the lower planetary boundary layer (PBL) While the nocturnal thermal inversion disappeared at around 18 UTC (Figure 6a), the dew point temperature increased at the lower PBL via synoptic moisture advection. The hourly observation from YMM (Fort McMurray airport) demonstrated the same trend of temperature and moisture increasing with slightly lower dew-point temperatures as model outputs.

The wind direction changed around 18 UTC from south westerlies to south easterlies in the burned area. The high bulk Richardson number of 93 (BRN) at 23 UTC (Figure 5) was an indicator of the small vertical wind shear and high CAPE; it was also an indicator of strong buoyant convection. The mid-level lifted index (LI, which is an index used to assess low level parcel stability) changed from positive (1.5) to negative (-4.7) during the same period of time. A negative LI indicates that the PBL is unstable with respect to the middle troposphere. An LI magnitude of -4 to -7 is classified as a large, unstable BPL. This is an environment in which convection/pyroconvection can occur. The more negative the LI, the more unstable the atmosphere will be for a rising parcel of air from the PBL. At the same time, the lifting condensation level (LCL) and level of free convection (LFC) merge at the 800 mb pressure level (2–2.5 km above the ground) with an equilibrium level (EL) about 270 mb or 11 km above ground level. Our simulation indicated that the pyro-cumulus cell onset was as late as 21 UTC on May 2, when the CAPE reached 650 J kg^{-1} , and the convection inhibition (CIN, which is the energy that is needed to lift an air parcel upward adiabatically to the LCL) was 0 J kg^{-1} . The dew-point temperature of the atmosphere profile above 50 kPa increased to a maximum of 10 °C around 8 km above-ground in less than 13 h (Figure 6a,b, green line). Moistening the entire atmospheric profile increased the atmospheric buoyancy.

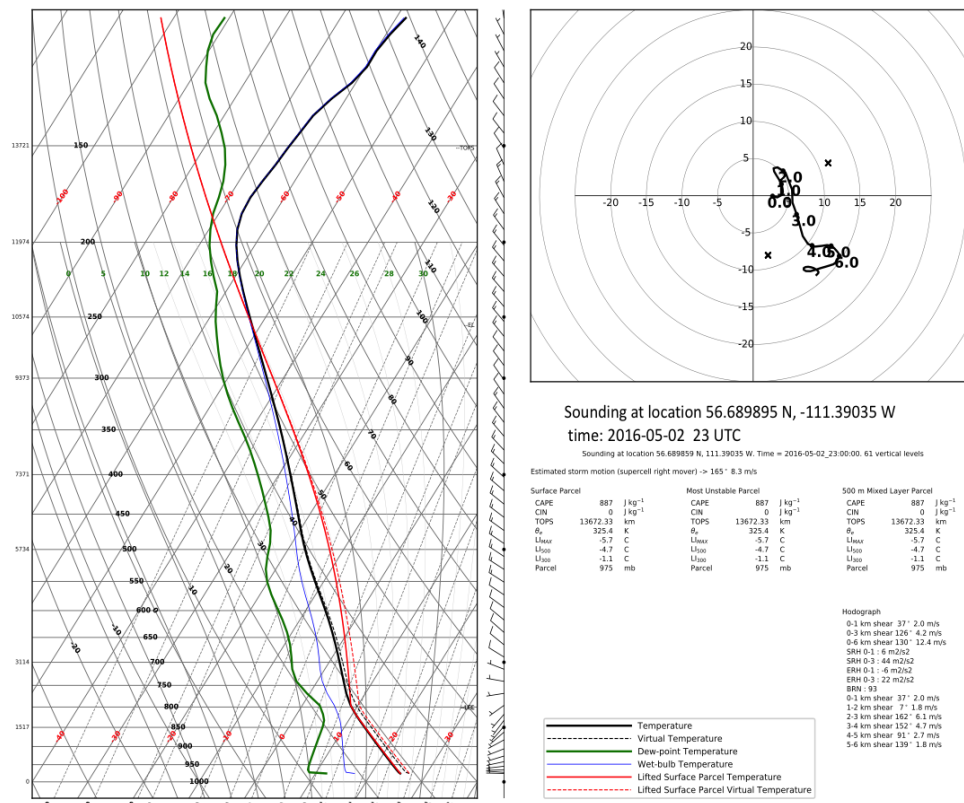


Figure 5. Model sounding and hodograph at the location 56.689895 N, 111.39035 W. The convective available potential energy (CAPE) reached 887 J/kg with no convection inhibition (CIN). The mean wind determined the speed and direction of the main pyroconvection cell at 23:00 UTC on May 2. The solid black line in Skew-T is the ambient air temperature, the solid green line is the dew-point temperature and the solid red line is the lifted surface parcel temperature.

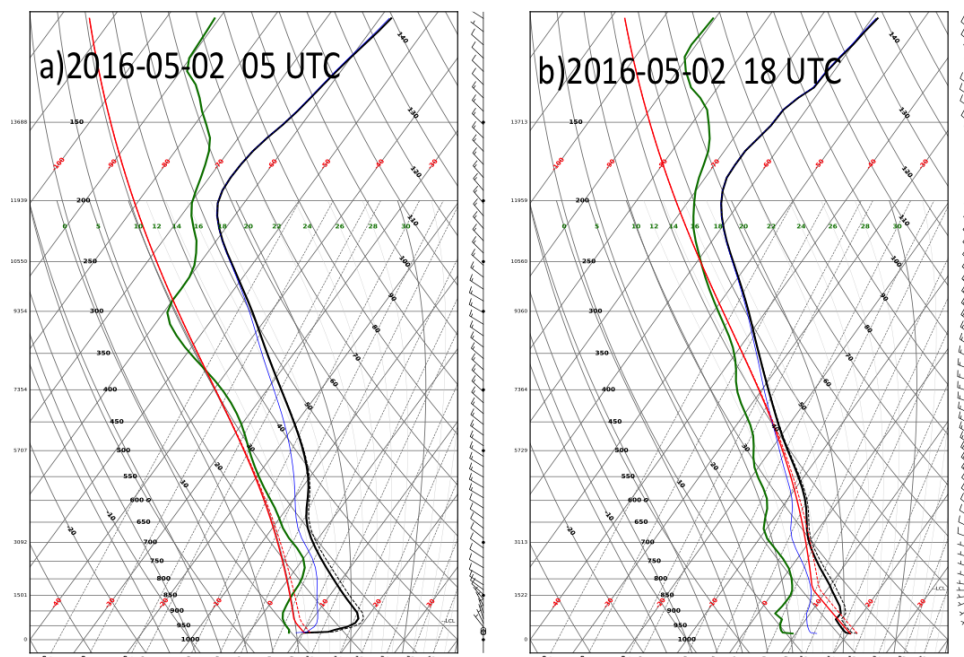


Figure 6. Model sounding at the location 56.689895 N, 111.39035 W at (a) 05 UTC on May 2 and (b) 18 UTC on May 2. The solid black line in Skew-T is the ambient air temperature, the solid green line is the dew-point temperature and the solid red line is the lifted surface parcel temperature.

Figure 7 gives a demonstration of three cross-sections at the grid points [170, 186], where the highest heat flux and wind speed occurred. The figure includes three snapshots at 00 UTC on May 3, 2016 in three different vertical planes at 163, 0 and 90° from north at the the grid point with the highest wind speed. Figure 7a is identical to a classical MCS cross-section with two downdraft areas behind and in front of the main updraft cell. The extension of the updraft 5 km above ground level shows the extension of pyro-cumulus in the back and front of the main cell. The two other cross-sections (Figure 7b,c) are the meridional and zonal views of the cell at 00 UTC on May 3, 2016. The pyroconvection activity slowed above the freezing level, but updrafts stretched to the top of the troposphere (Figure 7b,c). The vertical updraft reached the tropopause as early as 6 h after the fire ignition in the model (not shown here).

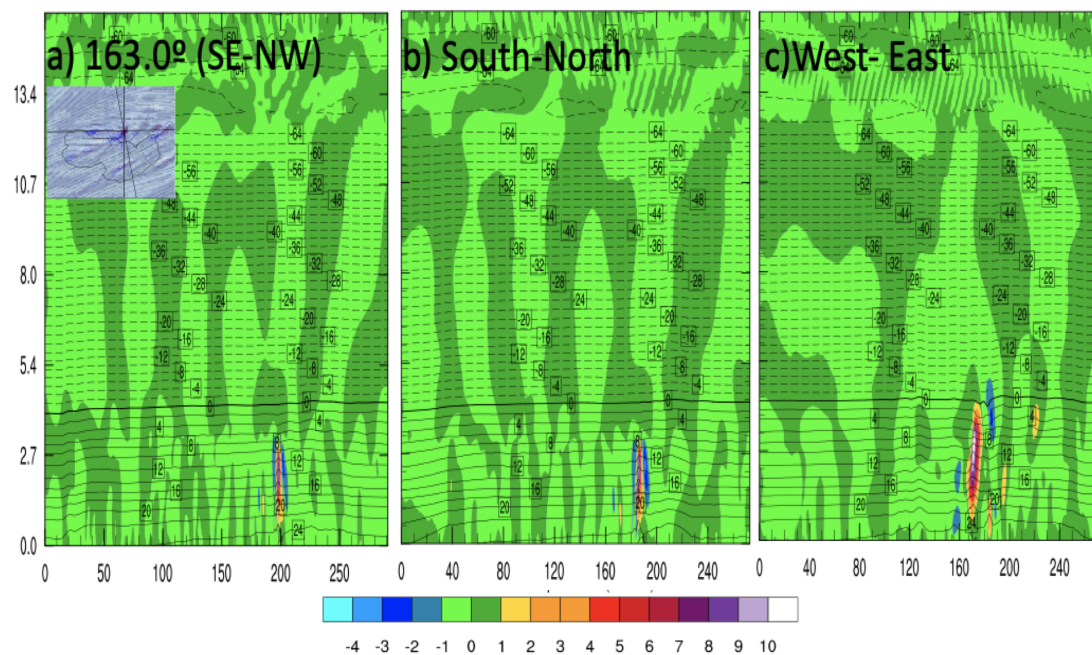


Figure 7. Vertical wind speed at 00 UTC on May 3, 2016. The resolution is 200 m in (a). The slightly tilted vertical plane is in the direction of lower-level (0–6 km) wind-shear, with the presentation of all three vertical cross-sections orientations with the colored horizontal vorticities on the burning area perimeter (left corner of image). (b) Meridional cross-section; (c) zonal cross-section passing through the maximum updraft location (170,186 grids). The vertical axes are the height in km, and horizontal axes are the number of grid points with 200 m resolution.

Figures 8 and 9 are two close-ups of the horizontal planes at model levels 1 (second level of 60 model levels) and 10 (boundary layer). Figure 8 displays a detailed perspective of horizontal wind, temperature and humidity slightly above-ground within the center of the pyroconvection updrafts and downdrafts. Figure 9 is similar to Figure 8 at model level 10, located around 2.5–3 km above the ground. The comparison of the vertical and horizontal views indicates the developed cells, associated downdrafts, dry air, wind convergence and divergence locations. The thermal gradient aloft reached 2 °C at 3.5 km above the ground (Figure 9b). The thermal gradient created strong convergence and divergence areas, strong surface winds, updrafts and downdrafts (Figure 8a and 9a). The updraft reached a magnitude above 11 m/s at around 4 km of altitude (Figure 7c), which is well above the LFC (Figure 5). The unstable PBL with the fire wind created large cells of pyrocumulus. The downdrafts of the main cell created smaller cells in the direction of the lower-level (0–6 km above the ground) vertical mean wind. On the other hand, the heat fluxes from the fire front created a horizontal thermal gradient as large as 10 °C in a distance of less than 200 m (Figure 8b) at the surface.

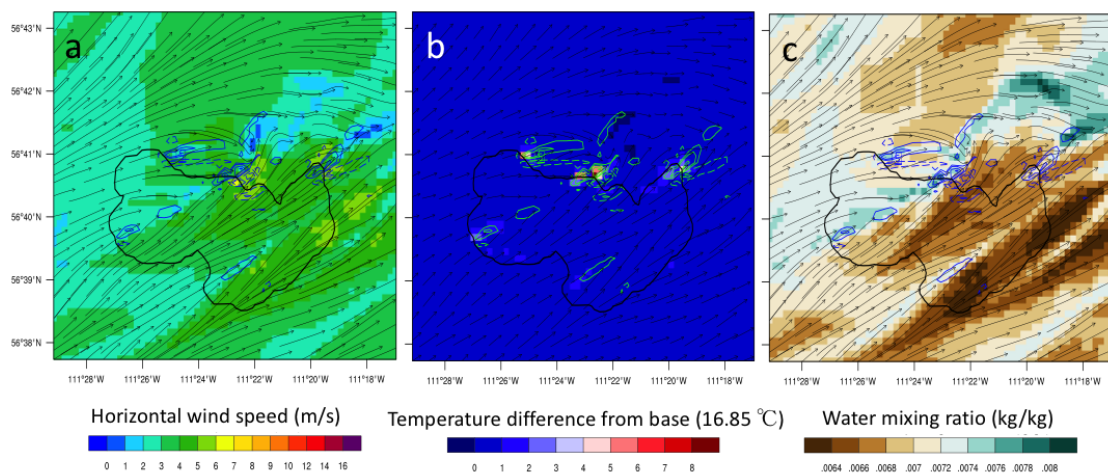


Figure 8. Horizontal snap shot at model level 1 (200–500 m above ground) on May 3, 2016 00 UTC of (a) wind speed and direction, (b) temperature gradient and wind direction and (c) mixing ratio and wind direction. The blue contour lines represent the vertical velocities. The dashed contours represent downdrafts, and solid line contours represent updrafts. The black line illustrates the fire perimeter.

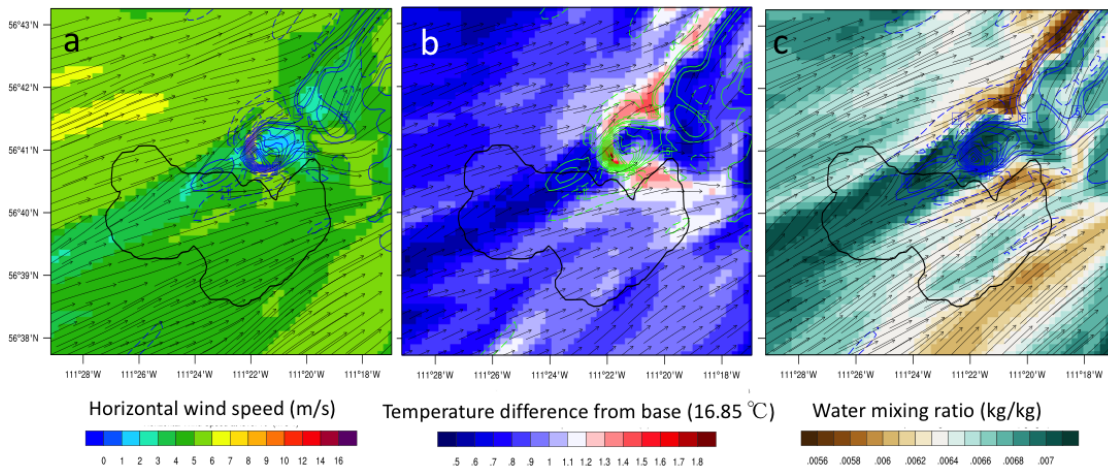


Figure 9. Horizontal snap shot at model level 10 (3000–3500 m above ground) on May 3, 2016 00 UTC of (a) wind speed and direction, (b) temperature gradient and wind direction and (c) mixing ratio and wind direction. The blue contour lines represent the vertical velocities. The dashed contours represent downdrafts, and solid line contours represent updrafts. The black line illustrates the fire perimeter.

Figure 10 demonstrates the burned area on May 1 and 2. Figure 10a presents the WRF-Fire burned area outputs at 00 UTC on May 3. The overlay of the May 2, hotspots and WRF-Fire burned areas is acceptably matched. WRF-Fire outputs gave a demonstration of the rate of spread, the fire perimeter as wind direction changed and pyroconvection activities. They captured the change of wind direction and timing when the eastward fire front slowed down and the fire progressed westwards towards the river. The simulated fire front shifted almost 2 km west of the actual fire perimeter in this simulation on the west and east sides. The bias is mainly due to the ignition locations, time and biomass map resolution, which is discussed in Appendix A.

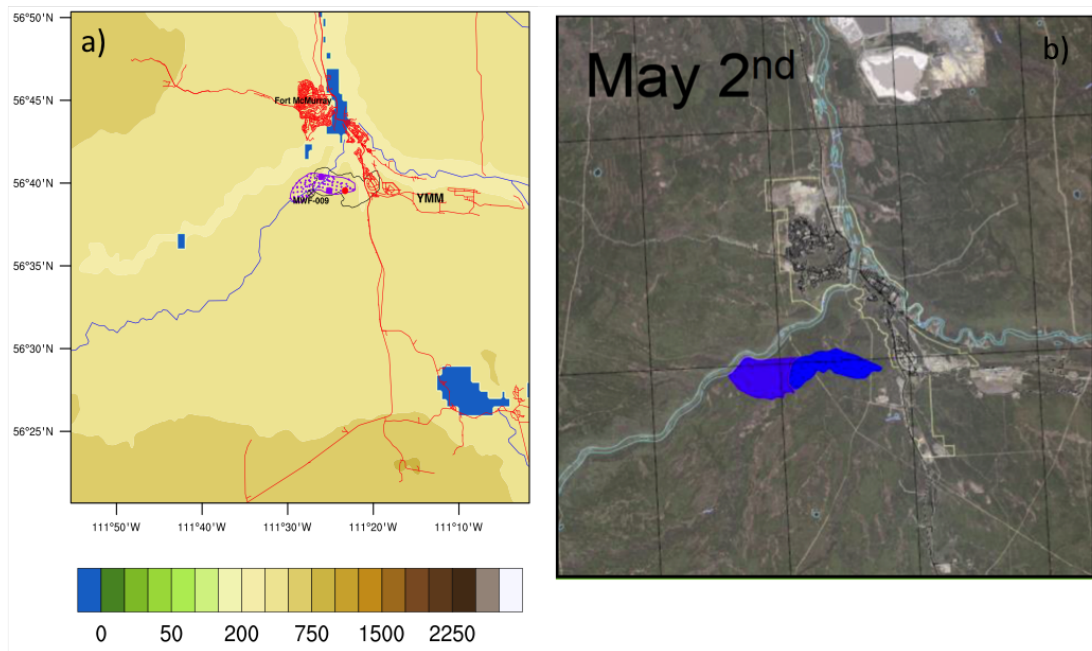


Figure 10. Burned area: left: overlay of WRF inner domain topography, burned area model output (black line), WRF ignitions (large purple and red circles), the earliest reported fire (MWF009-16) black circle and all detected 24 h hotspots on May 2, 2016. Right: burned area, courtesy of MWF-009-16, Alberta Parks report. The blue color presents the burned area on May 1. The dark purple-bluish shade is the burned area on May 2.

The NASA image on May 3, 2016 (Figure 11) demonstrates the large pyrocumulus cloud over the area with a distinguished rotation and overshooting area. Figure 12 shows two different views of the Horse River wildfire at early development time (23:51 UTC May 1). The updraft and downdraft can be identified at early stages. There is no report on lightning during this fire (a strong downdraft can produce more fires via lightning).



Figure 11. NASA (Aqua/Moderate Resolution Imaging Spectroradiometer (MODIS)) image on May 3.

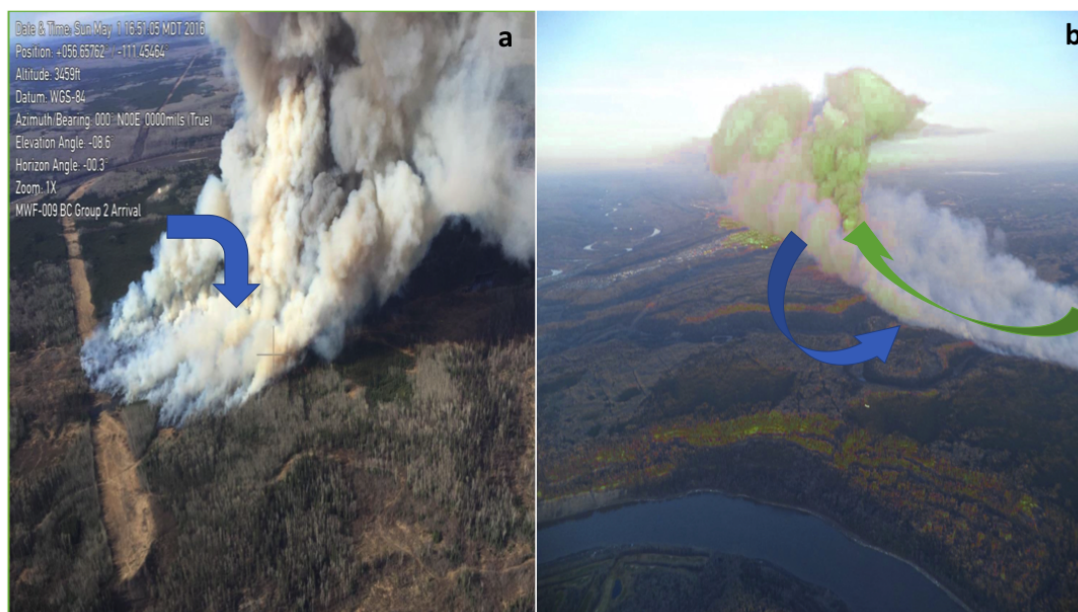


Figure 12. Horse River fire at 16:51 MDT, May 1, 2016 (less than one hour after detection). Fire Images are courtesy from MWF-009-16, Alberta Parks report. (a) West view of Horse River fire (May 1, 2016 23:51), (b) east view of Horse River fire, with green shade to demonstrate the strong updraft area. The blue arrows are the illustration of downdrafts and green arrow shows updraft.

5. Conclusions

Despite the shortcomings of initialization (hotspot acquisitions) and high-resolution vegetation and biomass fuel data, we were successful in simulating the pyroconvection activity with good accuracy in a timely manner. The 24 h simulation was completed in 6 h using 144 computational processing units (CPUs) from the resources of Compute Canada. We captured the increased horizontal wind speed and updraft, moisture fluxes, strong thermal gradient, updraft and onset of pyroconvection. None of the above could be captured with an atmosphere or wildfire model. A coupled atmosphere–wildfire model is required.

The use of the vertical atmosphere profile is crucial to foresee the onset of pyroconvection, unstable atmosphere and buoyancy. Model outputs can be a suitable substitute for the atmospheric profile around a burning area where there is no sounding. The simulation demonstrated that the combination of the day-time elimination of nocturnal capping inversion, Horse River wildfire pyroconvection (increasing heat and moisture at the surface) and moisture advection increased the CAPE. The 887 J/kg total increases of CAPE in less than 5 h and the high bulk Richardson number of 93 (BRN) were indicators of the growing pyro-cumulus cell. The simulation showed the adequacy of the current WRF-Fire approach for real-time applications.

We have made an effort to overcome all compatibility, technicality and mismatch issues between different data sources and the WRF-Fire model, such as adapting the Canadian biomass fuel classification for WRF-Fire. However, there is a larger stumbling block to overcome on the road to an operational coupled model. Wildfires and associated problems are classified as ground-based issues, which are managed by provincial, territorial or state levels of governments. Unlike fire, the atmosphere is a concern for national and international organizations and management levels. The separation of authorities and their abilities into the two key fields is an obstacle on the road to an operational coupled atmosphere–wildfire model that requires actions and collaborations from outside of scientific communities. While it sounds simple to add a fire model to a weather model (and it has been done in the past), in a complicated and well established organized NWP developing centre, no national or international weather forecasting center has crossed into the area of wildfire forecasting. As a result, natural resource organizations with limited meteorological staff or developers

focus on 2D spread models, and weather prediction organizations use a dispersion model approach for wildfire emission forecasts with biases due to a lack of wildfire heat, moisture and emissions coupling. Similar to weather and climate, wildfires know no national boundaries; thus, national and international cooperation at a large scale is essential for the development of an advanced operational coupled atmosphere–wildfire prediction system equipped with data assimilation and numerical weather forecast experts. Wildfire management is done mainly by provincial authorities in Canada, and they receive national help in times of emergency at their request. However, it unclear how they can foresee the requirement help without an accurate prediction method. No province in Canada has the potential to adopt an operational coupled weather–wildfire model simply because of the lack of an operational numerical weather prediction (NWP) center with data assimilation capacity and sufficient expertise. The temporary solutions in the past, such as short-term contracts, graduate research grants and IT developers, did not result in an evolving operational solution that can be updated with advancements in observation and fire science.

Regarding the areas of improvement within the current paper, we recognize that the verification of a model is not scientifically possible at this time due to limited data and accessibility. We also realize that satellite fire detection has limitations including time lapses, false alarms and undetected fires or misrepresentations of the actual burned area and fire size. Additionally, we found that the fuel classification can be improved by using a dynamic approach with high-resolution vegetation satellite images; this will be another research topic in future. The uncertain initialization and initial conditions lead to biased results, and the bias increases by the lead time in simulation. Advancements in initialization improve the overall outcomes.

Author Contributions: Conceptualization, A.B.; Funding acquisition, E.A.J.; Investigation, A.B. and K.N.; Project administration, A.B.; Resources, A.B. and K.N.; Writing—original draft, A.B.; Writing—review & editing, E.A.J. and K.N. All authors have read and agreed to the published version of the manuscript

Funding: This work would not be possible without the financial support of EYES HIGH of the University of Calgary and the Natural Sciences and Engineering Research Council of Canada.

Acknowledgments: The authors would like to thank Kerry Anderson and Bo Lu from Natural Resources of Canada for their support regarding the Canadian Digital fuel map. Many thanks to Kiyoko Miyanishi for improving the manuscripts. The authors would like to thank Cordy Tymstra from Alberta Agriculture and Forestry for the facilitation of communication and information. Finally, we would like to thank the Carroll family for their extended support during the Covid-19 pandemic in NB, Canada.

Conflicts of Interest: The authors declare no conflict of interest.

Abbreviations

The following abbreviations are used in this manuscript:

| | |
|------|---|
| BRN | Balk Richardson Number |
| CAPE | Convective Available Potential Energy |
| CCL | Convective Condensation Level |
| CIN | Convection Inhibition |
| LCL | Lifting Condensation Level |
| MCS | Mesoscale Convection Systems |
| NWP | Numerical Weather prediction |
| PBL | Planetary Boundary Layer |
| PMCS | Pyroconvection Mesoscale Convection Systems |

Appendix A. Fuel and Topography

We used the Canadian Digital Fuel map provided by Natural Resources of Canada. The resolution of the raster fuel map is 250 m. Data sources include the Land Cover Time Series (2011), Canadian Forest Inventory (CanFI2000), and British Columbia’s Biogeoclimatic Ecosystems Classification (Canadian National FBP Fuels 2014). The geo-referenced GeoTIFF files were converted into the Geogrid binary file format for WRF-Fire. Prior conversions were based on the OpenWFM.org guide. The desirable

fuel resolution should be finer or on the same order as the fire grid resolution, which in this case is 20 m. Topographic factors emphasize the terrain slope but also include orientation toward the sun and barriers that can interrupt the fire spread, such as creeks and roads that lead to airflow effects such as gap winds. Topography data at 3 s across North America represent the finest default resolution of land-use and topography in WRF. We used a finer resolution of 20 m from the Canadian Digital Elevation Model (this can be obtained from the Government of Canada's Geospatial Data Extraction website, <http://maps.canada.ca/czs/index-en.html>).

The fine-resolution elevation data for the fire grid were transferred to a variable called ZSF and also overwritten with HGT_M only where high-resolution DEM data are available. The multi-nested domain does not require fine-resolution data for coarser-resolution domains. The above arrangement leads to topography variables being accessible for all domains.

After the topography and fuel data are properly converted and provided for WRF-Fire, the WPS interpolates initial and boundary conditions for WRF. To simulate fire and weather, the WRF and its fire module need further amendment and set-up. The user-defined "namelist" files in WPS and WRF are a key part of setting up the simulation (see documentation on openwfm.org). The fuel properties for the fire module were defined in a file called "namelist.fire" [16]. To simplify the specification of fuel properties, the vectors of values of the fuel properties were given to each one of 13 Anderson [19] categories. We modified "namelist.fire" for Canadian fuel, including 22 categories. The adjustment requires the assignment of a vector of values for each fuel class. The nine values that required adjustments for 22 Canadian fuel categories were as follows:

1. windrf—Wind reduction factor from 20ft to mid-flame height (1);
2. fgi—The initial mass loading of surface fuel (kg m^{-2}) in each fuel category;
3. fueldepthm—Fuel depth (m);
4. savr—Fuel surface-area-to-volume-ratio (m^{-1});
5. fuelmce—Fuel moisture content of extinction (kg/kg);
6. fueldens—Fuel particle density lb ft^{-3} (32 if solid, 19 if rotten);
7. st—Fuel particle total mineral content (kg minerals/kg wood);
8. se—Fuel particle effective mineral content ((kg minerals – kg silica)/kg wood);
9. weight—Weighting parameter that determines the slope of the mass loss curve—this can range from about 5 (fast burnup) to 1000 (40% decrease in mass over 10 min).

While there have been no estimations or previous studies to define a definite parameter set for Canadian fuel categories, we adjusted the number according to our best knowledge [19,21,22]. There is a need to find more empirical values for each fuel class; however, the current values that we used would not impact the current case study for two reasons: (1) the fuel in the domain of study is limited to the four classes of C1(spruce–lichen woodland), C2 (boreal spruce), D1(leafless aspen), M1 (boreal mixed wood) and non-fuel such as classes 18, 19 and 21 (which are water, urban and non-fuel). The fuel resolution map also is 250 m, which is 10 times larger than fire grid resolution; (2) Coen et al. [23] found that reducing the fuel load by one-half reduced the forward rate of spread by one-fifth; doubling the load increased the spread rate by two-fifths. They explained the reason for this as follows: "horizontal winds decelerate as they are redirected up into the plume. However, near-fire horizontal winds determining the fire rate of spread could not vary in proportion to the fuel load across the experiments". Although the correct values impact the released fluxes and deep vertical activity, the impact of vertical behavior with the current available data will not be measurable. Increased data sensitivity and research on the fuel model could produce a better estimation.

References

1. Gillett, N.; Weaver, A.; Zwiers, F.; Flannigan, M. Detecting the effect of climate change on Canadian forest fires. *Geophys. Res. Lett.* **2004**, *31*. [[CrossRef](#)]

2. Trouet, V.; Taylor, A.H.; Wahl, E.R.; Skinner, C.N.; Stephens, S.L. Fire and climate interactions in the American West since 1400 CE. *Geophys. Res. Lett.* **2010**, *37*. [[CrossRef](#)]
3. Johnson, E.; Miyanishi, K. (Eds.) . Forest Fires. Academic Press: San Diego, CA, USA 2001; pp. 594. [[CrossRef](#)]
4. Yongqiang, L.; Scott, G.; Warren, H. Wildland fire emissions, carbon, and climate: Wildfire—Climate interactions. *For. Ecol. Manag.* **2014**, *317*, 80–96. [[CrossRef](#)]
5. Urbanski, S. Wildland fire emissions, carbon, and climate: Emission factors. *For. Ecol. Manag.* **2014**, *317*, 51–60. [[CrossRef](#)]
6. Landis, M.S.; Edgerton, E.S.; White, E.M.; Wentworth, G.R.; Sullivan, A.P.; Dillner, A.M. The impact of the 2016 Fort McMurray Horse River Wildfire on ambient air pollution levels in the Athabasca Oil Sands Region, Alberta, Canada. *Sci. Total. Environ.* **2018**, *618*, 1665–1676. [[CrossRef](#)] [[PubMed](#)]
7. Yue, X.; Unger, N. Fire air pollution reduces global terrestrial productivity. *Nat. Commun.* **2018**, *9*, 5413. [[CrossRef](#)] [[PubMed](#)]
8. Trentmann, J.; Luderer, G.; Winterrath, T.; Fromm, M.D.; Servranckx, R.; Textor, C.; Herzog, M.; Graf, H.F.; Andreae, M.O. Modeling of biomass smoke injection into the lower stratosphere by a large forest fire (Part I): reference simulation. *Atmos. Chem. Phys.* **2006**, *6*, 5247–5260. [[CrossRef](#)]
9. Williams, A.P.; Seager, R.; Berkelhammer, M.; Macalady, A.K.; Crimmins, M.A.; Swetnam, T.W.; Trugman, A.T.; Buening, N.; Hryniw, N.; McDowell, N.G.; et al. Causes and Implications of Extreme Atmospheric Moisture Demand during the Record-Breaking 2011 Wildfire Season in the Southwestern United States. *J. Appl. Meteorol. Climatol.* **2014**, *53*, 2671–2684. [[CrossRef](#)]
10. Randel, D.L.; Vonder Haar, T.H.; Ringerud, M.A.; Stephens, G.L.; Greenwald, T.J.; Combs, C.L. A New Global Water Vapor Dataset. *Bull. Am. Meteorol. Soc.* **1996**, *77*, 1233–1246. Available online: [http://xxx.lanl.gov/abs/https://journals.ametsoc.org/bams/article-pdf/77/6/1233/3728952/1520-0477\(1996\)077_1233_angwvd_2_0_co_2.pdf](http://xxx.lanl.gov/abs/https://journals.ametsoc.org/bams/article-pdf/77/6/1233/3728952/1520-0477(1996)077_1233_angwvd_2_0_co_2.pdf), Jun 1,2020. [[CrossRef](#)]
11. Läderach, A.; Sodemann, H. A revised picture of the atmospheric moisture residence time. *Geophys. Res. Lett.* **2016**, *43*, 924–933. Available online: <https://agupubs.onlinelibrary.wiley.com/doi/pdf/10.1002/2015GL067449>, Jun 1,2020. [[CrossRef](#)]
12. Lareau, N.; Clements, C. Environmental controls on pyrocumulus and pyrocumulonimbus initiation and development. *Atmos. Chem. Phys.* **2016**, *16*, 4005–4022. [[CrossRef](#)]
13. Stull, R. *Practical Meteorology*; The University of British Columbia: Vancouver, BC, Canada, 2016; pp. 488–496.
14. Badlan, R.; Sharplesa, J.; Evans, J.; McRae, R. The role of deep flaming in violent pyroconvection. In Proceedings of the 22nd International Congress on Modelling and Simulation, Hobart, Tasmania, 3–8 December 2017; pp. 1090–1096.
15. Bakhshaii, A.; Johnson, E. A review of a new generation of wildfire–atmosphere modeling. *Can. J. For. Res.* **2019**, *49*, 565–574. [[CrossRef](#)]
16. Mandel, J.; Beezley, J.D.; Kochanski, A.K. Coupled atmosphere-wildland fire modeling with WRF 3.3 and SFIRE. *Geosci. Model Dev.* **2011**, *4*, 591–610. [[CrossRef](#)]
17. Mandel, J.; Fournier, A.; Jenkins, M.; Kochanski, A.; Schranz, S.; Vejmelka, M. Assimilation of Satellite Active Fires Detection Into a Coupled Weather-Fire Model. In Proceedings of the 5th International Fire Behavior and Fuels Conference; International Association of Wildland Fire, Melbourne, Australia, 11–15 April 2016.
18. Rothermel, R. A mathematical model for predicting fire spread in wildland fuels. *Res. Pap. INT* **1972**, *115*.
19. Anderson, H.E. *Aids to Determining Fuel Models for Estimating Fire Behavior*; Gen. Tech. Rep. INT-122; U.S.Department of Agriculture, Forest Service, Intermountain Forest and Range Experiment Station: Ogden, UT, USA, 1982; p. 22.
20. Giglio, L.; Descloitres, J.; Justice, C.O.; Kaufman, Y.J. An Enhanced Contextual Fire Detection Algorithm for MODIS. *Remote. Sens. Environ.* **2003**, *87*, 273–282. [[CrossRef](#)]
21. Forestry. *Development and Structure of the Canadian Forest Fire Behavior Prediction System*; Forest Service Publications: Quebec, QC, Canada 1992; p. 63. URL: <https://cfs.nrcan.gc.ca/publications?id=10068>

22. Anderson, K. A model to predict lightning-caused fire occurrences. *Int. J. of Wildland Fire* **2002**, *11*, 163–172. [[CrossRef](#)]
23. Coen, J.; Cameron, M.; Michalakes, J.; Patton, E.; Riggan, P.; Yedinak, K. Coupled Weather and Wildland Fire Modeling with the Weather Research and Forecasting Mode. *J. Appl. Meteor. Climatol.* **2013**, *52*, 16–38. [[CrossRef](#)]



© 2020 by the authors. Licensee MDPI, Basel, Switzerland. This article is an open access article distributed under the terms and conditions of the Creative Commons Attribution (CC BY) license (<http://creativecommons.org/licenses/by/4.0/>).